




Article

Optimal Icosahedral Copper-Based Bimetallic Clusters for the Selective Electrocatalytic CO₂ Conversion to One Carbon Products

Azeem Ghulam Nabi ^{1,2,3,4,*}, Aman-ur-Rehman ^{2,5,6}, Akhtar Hussain ⁴, Gregory A. Chass ^{1,7,8} and Devis Di Tommaso ^{1,*} 

- ¹ Department of Chemistry, School of Physical and Chemical Sciences, Queen Mary University of London, Mile End Road, London E1 4NS, UK
- ² Department of Physics and Applied Mathematics, Pakistan Institute of Engineering and Applied Sciences, Nilore, Islamabad 45650, Pakistan
- ³ Department of Physics, University of Gujrat, Jalalpur Jattan Road, Gujrat 50700, Pakistan
- ⁴ Theoretical Physics Division, Pakistan Institute of Nuclear Science & Technology (PINSTECH), Nilore, Islamabad 45650, Pakistan
- ⁵ Department of Nuclear Engineering, Pakistan Institute of Engineering & Applied Sciences, Nilore, Islamabad 45650, Pakistan
- ⁶ Center for Mathematical Sciences, Pakistan Institute of Engineering & Applied Sciences, Nilore, Islamabad 45650, Pakistan
- ⁷ Department of Chemistry, McMaster University, Hamilton, ON L8S 4L8, Canada
- ⁸ Faculty of Land and Food Systems, The University of British Columbia, Vancouver, BC V6T1Z4, Canada
- * Correspondence: g.azeem@qmul.ac.uk (A.G.N.); d.dtommaso@qmul.ac.uk (D.D.T.)

Abstract: Electrochemical CO₂ reduction reactions can lead to high value-added chemical and materials production while helping decrease anthropogenic CO₂ emissions. Copper metal clusters can reduce CO₂ to more than thirty different hydrocarbons and oxygenates yet they lack the required selectivity. We present a computational characterization of the role of nano-structuring and alloying in Cu-based catalysts on the activity and selectivity of CO₂ reduction to generate the following one-carbon products: carbon monoxide (CO), formic acid (HCOOH), formaldehyde (H₂C=O), methanol (CH₃OH) and methane (CH₄). The structures and energetics were determined for the adsorption, activation, and conversion of CO₂ on monometallic and bimetallic (decorated and core@shell) 55-atom Cu-based clusters. The dopant metals considered were Ag, Cd, Pd, Pt, and Zn, located at different coordination sites. The relative binding strength of the intermediates were used to identify the optimal catalyst for the selective CO₂ conversion to one-carbon products. It was discovered that single atom Cd or Zn doping is optimal for the conversion of CO₂ to CO. The core@shell models with Ag, Pd and Pt provided higher selectivity for formic acid and formaldehyde. The Cu-Pt and Cu-Pd showed lowest overpotential for methane formation.

Keywords: CO₂ reduction; copper catalysts; metal doping; density functional calculations



Citation: Nabi, A.G.; Aman-ur-Rehman; Hussain, A.; Chass, G.A.; Di Tommaso, D. Optimal Icosahedral Copper-Based Bimetallic Clusters for the Selective Electrocatalytic CO₂ Conversion to One Carbon Products. *Nanomaterials* **2023**, *13*, 87. <https://doi.org/10.3390/nano13010087>

Academic Editor: Shiqiang (Rob) Hui

Received: 16 November 2022

Revised: 19 December 2022

Accepted: 20 December 2022

Published: 24 December 2022



Copyright: © 2022 by the authors. Licensee MDPI, Basel, Switzerland. This article is an open access article distributed under the terms and conditions of the Creative Commons Attribution (CC BY) license (<https://creativecommons.org/licenses/by/4.0/>).

1. Introduction

The rising carbon dioxide (CO₂) level and overall concentrations in the atmosphere due to fossil fuel combustion, a major cause of global warming, pose a serious threat to humankind [1]. One of the most promising solutions to mitigating this risk is via the chemical conversion of gaseous CO₂ into value-added chemicals and materials [2]. The electrochemical CO₂ reduction reaction (eCO₂RR) has emerged as a potential strategy for converting CO₂ because if coupled with electricity from renewable sources (wind, solar, or hydropower plants), the eCO₂RR could achieve a carbon-neutral energy cycle [3,4]. The main challenges in eCO₂RR lie in the activation of competitive CO₂-minimizing pathways such as the hydrogen evolution reaction (HER, $H^+ + e^- \rightarrow \frac{1}{2} H_2$) [5,6] and the conversion

of CO₂ to a specific product with good selectivity; this given the marginal difference in the electrochemical potentials of CO₂ reduction into different products [3]. For example, the change for transforming CO₂ to ethylene is -0.34 V while the CO₂ to methanol transformation is -0.38 V, relative to the standard hydrogen electrode (SHE) [7].

Catalysts can facilitate favorable pathways to reduce the overall energy requirements of eCO₂RR. Due to their ability to activate CO₂, initial research focused on noble metal-based catalysts (Pt, Rh, Ir) [8–12], yet their scarcity and cost have retarded development. Hence, earth-abundant and active metal-based catalysts have been become requisite to develop sustainable solutions to CO₂ transformation, when all aspects are considered (i.e., fundamental chemistry/physics, technological, economical). Copper (Cu) emerges as the best candidate for eCO₂RR, being the only metal surface that reduces CO₂ to more than thirty hydrocarbons and oxygenates [13], yet lacks the required selectivity [14–16]. Relevant studies dedicated to improving selectivity and hindering the HER have investigated the adsorption/desorption mechanism on single crystal Cu electrodes to demonstrate the role of surface morphology [17]. It was discovered that Cu crystal facets with high index planes such as Cu(711) are more selective in the production of valuable two-carbon (C2) products, such as ethylene and ethanol. This with respect to the dominant Cu(111) surface [18], while stepped Cu surfaces such as the (211) facet more easily produce one-carbon (C1) hydrocarbons [19]. Computational studies also revealed that the higher activity of polycrystalline Cu nanoparticles is due to the presence of stepped facets, such as (110) [20], (211) [21] and Cu(321) [22]. These stepped surfaces occur in metal clusters [18,22–24], where both the number of uncoordinated sites at the corners and edges [25] and the surface-to-volume ratio of nanoparticles are higher than those on copper surfaces, which may lead to improved catalytic properties towards eCO₂RR [13].

Another strategy to improve the activity and selectivity of Cu electrodes is metal (M) doping [14]. Bimetallic catalysts often show better catalytic performance than the corresponding elemental metal ones due to synergic effects between the two metallic centers [26]. The dopant provides reaction sites with varied electronic properties and modulates those of the host (Cu), influencing the adsorption strength of the eCO₂RR intermediates. Experimental studies have also revealed that low doping concentrations facilitate the formation of C1 products [27,28]. In particular, metal dopants such as Ag [28,29], Cd [30], Pd [28,31], Pt [32], and Zn [28,33] in Cu-M catalysts show efficiency towards C1/C2 products.

Consequently, in Cu-based catalysts, the nanoscale structuring and cooperative metal-metal coupling could enhance CO₂ activation and selectivity, leading to specific product formation. In this regard, quantum mechanical modelling has provided insights into the structure, stability and catalytic properties of CuM clusters, while also demonstrating that an appropriate proportion of metal atoms influences the CO₂ activation and selectivity towards the desired reaction. Alvarez-Garcia et al. investigated the binding and dissociation of CO₂ on four-atom bimetallic Cu_nPd_{4-n} ($n = 0-4$) clusters employing density functional theory (DFT) calculations [30], resolving the ideal composition for adsorption energy and facile barriers to activation barrier was found in Cu₃Pd; in agreement with the Pd/(Pd + Cu) atomic ratioing reported experimentally [34,35]. Investigation on the effect of substituting Cu with Zr on CO₂ adsorption for the four-atom Cu₄ cluster [36] revealed that the energy barriers for the direct dissociation of the CO₂ molecule to CO + O decreased significantly for bimetallic CuZr clusters, with respect to pure Cu₄. Our recent computational work on small tetrahedral CuSn clusters revealed the Cu₂Sn₂ system to suppress the competitive HER, while being highly selective towards the electrochemical CO₂ → CO conversion [37]. Xing et al. considered bimetallic Pd_nCu_m ($m + n = 15$, with $n > m$) clusters wherein Pd₁₀Cu₅ showed the highest catalytic activity, particularly towards the CO₂ → COOH hydrogenation step [31]. Li et al. considered (Cu)_n clusters with $n = 8, 20, 38$ (even numbers) and $n = 13, 55$ (odd numbers) to investigate the reactivity at the high density corner and edge sites and found the icosahedral Cu₅₅ to provide the lowest energy pathway to the CO intermediate and the ensuing C2 ethylene product [25].

Computational characterizations of clusters in the size range of $10 \leq n \leq 55$ showed that $(\text{Cu})_n$ adopted the icosahedral structure [38] derived from 13- and 55-atom icosahedra, built by adding or removing atoms. In addition, a comparison of icosahedral and cuboctahedral ($n = 55, 147$ and 309) clusters confirmed the icosahedral copper clusters to be more stable. Experimental verification of the formation of copper clusters using microemulsion techniques revealed Cu_{55} to be one of the most abundant clusters followed by Cu_{13} , Cu_{147} and Cu_{309} [39]. According to a recent DFT investigation, Cu_{55} exhibits highly degenerate states [40]; a direct outcome of its icosahedral symmetry. Therefore, study on nanoclusters such as the highly symmetric 55-atom icosahedral structures would give a deeper understanding than stepped surfaces. This has been attributed to their larger surface-to-volume ratio and higher proportion of coordinatively unsaturated surface atoms (corner or edge) in comparison to bulk materials, resulting in a narrowing of the d-band, an upward shift of the band's energy, and consequently, a stronger adsorption of the reaction intermediates [41]. Investigation on the adsorption of CO_2 on icosahedral 55-atom Cu-based bimetallic clusters [42] found that for the $\text{Cu}_{55-x}\text{Zr}_x$ systems ($x = 1-12$), the formation of the CO_2 -activated state (linear to bent transition and elongation of C–O bonds) was endothermic on the pure copper cluster but barrierless and exothermic on the Zr-decorated system. Similarly, DFT calculations of $\text{Cu}_{55-x}\text{Zr}_x$ systems ($x = 0, 12, 13, 42, 43$ and 55) with a core@shell and decorated distribution of Cu and Ni atoms showed the presence of Ni on the clusters was crucial to the activation of CO_2 [43]. Although previous computational studies of icosahedral Cu-based bimetallic nanocatalysts considered the adsorption, activation and gas-phase dissociation of CO_2 , in the context of eCO_2RR , the focus should be on the concerted proton-electron transfer (CPET) steps [44].

Here, we present a computational investigation based on DFT calculations of the effect of nano-structuring and alloying in Cu-based catalysts on the activity and selectivity of the eCO_2RR . Starting from the icosahedral Cu_{55} structure, we generated Cu_{54}M_1 , $\text{Cu}_{43}\text{M}_{12}$ and $\text{Cu}_{30}\text{M}_{25}$ decorated architectures and $\text{Cu}_{13}\text{M}_{42}$ core@shell models ($\text{M} = \text{Ag}, \text{Cd}, \text{Pd}, \text{Pt}$, and Zn) (Figure 1), with the metals located at three different coordination sites (6, 8 and 12). We provide a thorough analysis of the structural, thermodynamic and electronic properties of these nanoclusters and their ability to activate CO_2 . The computational hydrogen electrode (CHE) model [45] was then applied to compute the mechanism of eCO_2RR to the C1 products carbon monoxide (CO), formic acid (HCOOH), formaldehyde (CH_2O), methane (CH_4) and methanol (CH_3OH). We have focused our attention to C1 products because a recent techno-economic assessment of low-temperature CO_2 electrolysis shows the production costs of C1 products such as HCOOH and CO are competitive to conventional processes compared to C2 products such as ethylene and ethanol, which production has substantially higher costs [46]. We compare the free energy profiles for the electrocatalytic CO_2 conversion to these C1 products to the competitive HER. The relative binding strength of the intermediates involved is used to identify catalysts for the selective CO_2 conversion. For comparison purposes, calculations of the eCO_2RR and HER were also conducted on the (100), (110), (111) and (211) facets of pure copper.

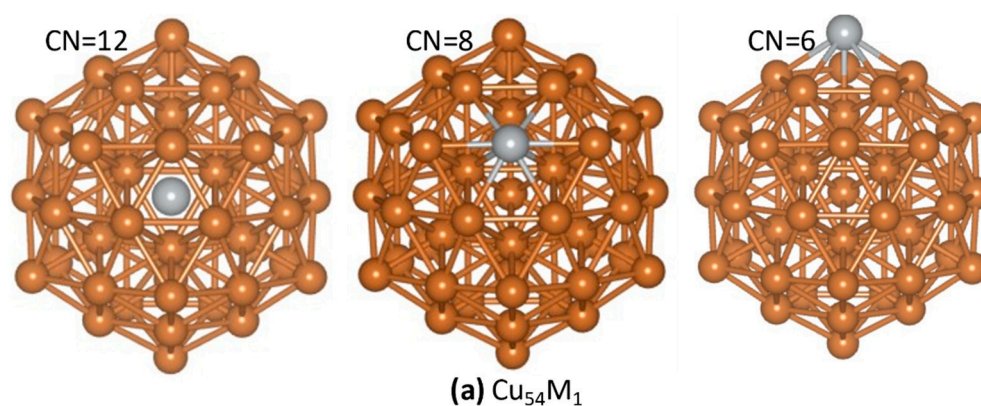


Figure 1. Cont.

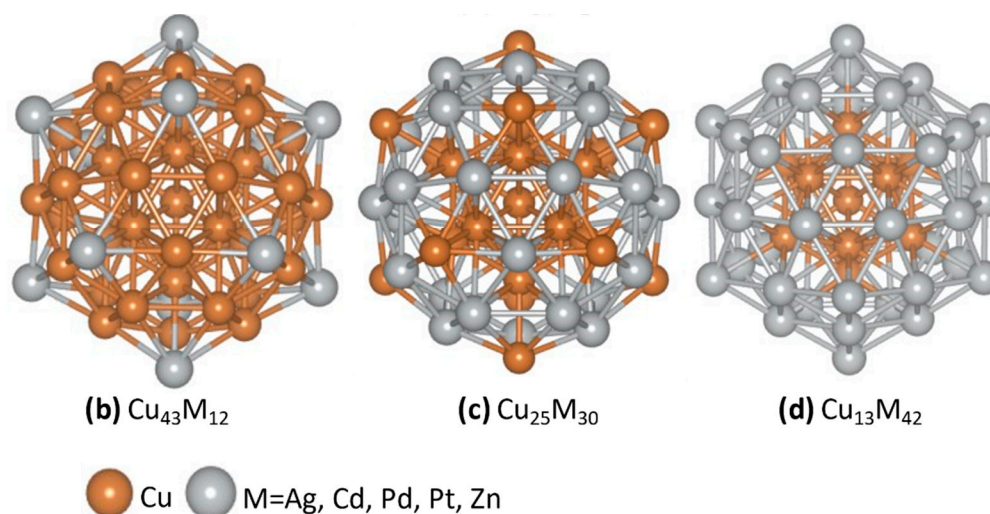


Figure 1. (a) The 55-atom Cu-based clusters doped with one metal atom (M) at three different coordination sites: CN = 6, 8 and 12. (b) The 55-atom Cu-based cluster doped with 12 metal atoms located at CN = 6. (c) The 55-atom Cu-based cluster doped with 30 metal atoms at CN = 8. (d) The core(Cu)@shell(M) cluster model.

2. Computational Methods

2.1. Atomistic Models of Clusters and Surfaces

The icosahedral (I_h) 55-atom monometallic Cu cluster was generated using the ab initio random structure searching (AIRSS) code [47]. The decorated Cu_{54}M clusters were then generated by replacing one surface Cu with a dopant metal atom M, where M = Ag, Cd, Pd, Pt and Zn. As shown in Figure 1a, there are three possible coordination sites: CN6 is the edge site, CN8 is the corner site and CN12 is the center of the nanocluster. The $\text{Cu}_{43}\text{M}_{12}$ model in Figure 1b was generated by replacing 12 Cu atoms with M located at CN6. The $\text{Cu}_{25}\text{M}_{30}$ model in Figure 1c was generated by replacing 12 Cu atoms with M located at CN8. The $\text{Cu}_{13}\text{M}_{42}$ core@shell model in Figure 1d was generated by replacing all 13 surface Cu atoms with M. We also considered four-layer (3×3) slab models of Cu(100), Cu(110), Cu(111) and Cu(211) [20] with the (100), (110) and (111) being the dominant surfaces of copper. The Cu(211) facet was considered because of its good selectivity towards C1 formation. This was linked to the Cu(211) morphology characterized by step-edge sites with a coordination number equal to 7 (CN7) [48]. Here, we have also compared the catalytic conversion of CO_2 to C1 chemicals on Cu(211) to that on 55-atoms icosahedral Cu-M nanoclusters with M located at CN6 and CN8.

2.2. Density Functional Theory Calculations

Calculations of energies and structures were conducted at the spin-polarized DFT level using the “Vienna ab initio simulation package” (VASP Software GmbH, version 6.3.1, Vienna, Austria) [49] using the following computational settings: the Perdew–Burke–Ernzerhof (PBE) exchange correlation functional with the Grimme’s-D3 dispersion correction; a plane-wave basis set within the framework of the projector augmented wave method with a kinetic energy cutoff (E_{cut}) set to 400 eV; a single k -point ($1 \times 1 \times 1$) for the nanoclusters and a ($5 \times 5 \times 1$) k -point mesh for the surface model to sample the Brillouin zone of the simulation supercell; a 0.18 eV width for the smearing. Energies, zero-point energies, and entropies of $\text{H}_2(\text{g})$, $\text{CO}_2(\text{g})$ and $\text{CO}(\text{g})$, and H_2O used to compute the free energy corrections are reported in Supplementary Information (Table S1).

2.3. Free Energy Calculations

Following the computational hydrogen electrode (CHE) method proposed by Nørskov and co-workers [45], the Gibbs free energy of each step involved in the eCO₂RR to C1 products was computed using the following equation:

$$\Delta G = \Delta S + \Delta E_{\text{ZPE}} - T\Delta S + \Delta G_{\text{solv}} + \Delta G_{\text{U}} \quad (1)$$

where ΔE is the reaction energy; ΔE_{ZPE} is the change in zero-point energy; ΔS is the change in entropy and T is the temperature of the reaction (300 K). We determined the latter two quantities within the harmonic approximation by taking the vibrational frequencies of adsorbates and molecules calculated with DFT. The solvation effects to compute the solvation free energy term ΔG_{solv} were included using VASPsol [50]. ΔG_{U} is the free energy correction introduced by the difference of the electrode potential. For reactions involving a concerted proton–electron transfer (CPET) step, the ΔG_{U} term can be computed by applying the formula:

$$\Delta G_{\text{U}} = -neU \quad (2)$$

where n is the number of electrons transferred, e is the electron charge and U is the applied electrode potential. The limiting potential (U_{L}) and the overpotential (η) are important factors for evaluating the catalytic activity. The limiting potential is given by the formula:

$$U_{\text{L}} = -\Delta G_{\text{max}}/ne \quad (3)$$

where ΔG_{max} is the relative change of the Gibbs free energy of the rate-determining step. The overpotential (η) can be obtained by calculating the difference between the equilibrium potential (U_{eq}) and the limiting potential:

$$\eta = U_{\text{eq}} - U_{\text{L}} \quad (4)$$

Thus, η represents the minimum applied potential required to facilitate the formation of relevant intermediates.

3. Results and Discussion

3.1. Stability, Structure, and Electronic Properties of the Icosahedral 55-Atom CuM Clusters

The segregation energy (SE) was used to determine the preference of the metal dopants (Ag, Cd, Pd, Pt and Zn) to be in the core or shell of Cu₅₄M. The SE is defined as [51]:

$$SE = E[\text{Cu}_{54}\text{M}(\text{surface})] - E[\text{Cu}_{54}\text{M}(\text{core})] \quad (5)$$

where $E[\text{Cu}_{54}\text{M}(\text{surface})]$ and $E[\text{Cu}_{54}\text{M}(\text{core})]$ are the electronic energies of the fully optimized Cu₅₄M₁ cluster obtained by replacing one Cu atom with a dopant metal at a surface (CN6 or CN8) and at the center of the cluster (CN12), respectively. In Figure 2, the SE values are negative for all Cu₅₄M, which implies that the metal prefers to be at the surface of the cluster, consistent with DFT calculations of Cu₅₄Zr [51]. The metal doping at the CN8 site is more stable than CN6, but because their values of SE were close, the adsorption and reduction of CO₂ on both coordination sites.

To gain insights into the relative stability of pure and bimetallic 55-atom systems, we used the binding energy per atom (E_{B}), defined as [52]:

$$E_{\text{B}} = \frac{E(\text{Cu}_{55-x}\text{M}_x) - (55 - x)E(\text{Cu}) - xE(\text{M})}{55} \quad (6)$$

where $E(\text{Cu}_{55-x}\text{M}_x)$ is the total energy of the most stable isomer of each Cu_{55-x}M_x cluster and $E(\text{Cu})$ and $E(\text{M})$ are the total energies of the Cu and Sn atoms, respectively. A higher negative value of E_{B} indicates higher thermodynamic stability of the cluster. The calculated E_{B} for pure Cu₅₅ nanocluster is −2.99 eV, equal to the value obtained using all-electron triple- ζ quality DFT calculations [53]. Table 1 reports the calculated E_{B} and other structural and

electronic properties: the average interatomic bonding distance between nearest neighbors, the energy difference between the highest occupied molecular orbital (HOMO), the lowest unoccupied molecular orbital (LUMO) (Δ_{H-L}), the Bader charge difference between the Cu and M atoms (ΔQ_M), and the surface energy (γ). The surface energy was computed using the following equation [54]:

$$\gamma = \frac{E_{\text{nanosphere}} - NE_{\text{bulk}}}{4\pi R^2} \quad (7)$$

where $E_{\text{nanosphere}}$ is the energy of a cluster with N atoms ($N = 55$), E_{bulk} is the energy of the bulk material per one layer of cross-section and R is the radius a spherical incorporating the cluster.

Table 1. The bond lengths (Å), formation energy (eV), HOMO-LUMO gap (Δ_{H-L} , eV), Bader charge difference (ΔQ_M , Coulomb), and surface energy (γ , eV) of the Cu and CuM (M = Ag, Cd, Pd, Pt and Zn) nanoclusters.

	Bond Length	Formation Energy	Δ_{H-L}	ΔQ_M	γ	
Pristine Cu ₅₅ Nanocluster						
Cu ₅₅	2.51	−2.99	—	—	−0.56	
1-atom doping on CN6						
Cu ₅₄ Ag ₁	2.69	−3.51	0.0001	−0.12	−0.56	
Cu ₅₄ Cd ₁	2.73	−3.48	0.0412	0.16	−0.54	
Cu ₅₄ Pd ₁	2.59	−3.53	0.1013	−0.37	−0.58	
Cu ₅₄ Pt ₁	2.56	−3.56	0.0441	−0.64	−0.59	
Cu ₅₄ Zn ₁	2.54	−3.48	0.0005	0.13	−0.58	
1-atom doping on CN8						
Cu ₅₄ Ag ₁	2.69	−3.52	0.0488	−0.08	−0.56	
Cu ₅₄ Cd ₁	2.73	−3.49	0.0349	0.14	−0.54	
Cu ₅₄ Pd ₁	2.59	−3.54	0.0431	−0.30	−0.58	
Cu ₅₄ Pt ₁	2.56	−3.57	0.0481	−0.63	−0.59	
Cu ₅₄ Zn ₁	2.54	−3.49	0.0414	0.17	−0.58	
12-atom doping on CN6						
Cu ₄₃ Ag ₁₂	2.67	−3.30	0.0858	−0.12	−0.51	
Cu ₄₃ Cd ₁₂	2.75	−2.90	0.0104	0.14	−0.42	
Cu ₄₃ Pd ₁₂	2.59	−3.59	0.0682	−0.32	−0.64	
Cu ₄₃ Pt ₁₂	2.56	−3.96	0.0824	−0.58	−0.68	
Cu ₄₃ Zn ₁₂	2.54	−2.98	0.1721	0.09	−0.49	
30-atom doping on CN8						
	Cu-M	M-M				
Cu ₂₅ Ag ₃₀	2.65	2.81	−2.93	0.0305	−0.06	−0.46
Cu ₂₅ Cd ₃₀	2.67	3.01	−1.95	0.0016	0.08	−0.26
Cu ₂₅ Pd ₃₀	2.59	2.70	−3.49	0.0568	−0.15	−0.71
Cu ₂₅ Pt ₃₀	2.59	2.69	−4.45	0.0524	−0.26	−0.82
Cu ₂₅ Zn ₃₀	2.53	2.75	−2.12	0.0980	0.09	−0.34
Core@shell						
Cu ₁₃ Ag ₄₂	2.81		−2.81	0.0835	−0.14	−0.40
Cu ₁₃ Cd ₄₂	2.95		−1.31	0.0131	−0.93	−0.15
Cu ₁₃ Pd ₄₂	2.68		−3.40	0.0168	0.78	−0.72
Cu ₁₃ Pt ₄₂	2.62		−4.72	0.0527	0.69	−0.86
Cu ₁₃ Zn ₄₂	2.56		−1.53	0.0173	−0.93	−0.23

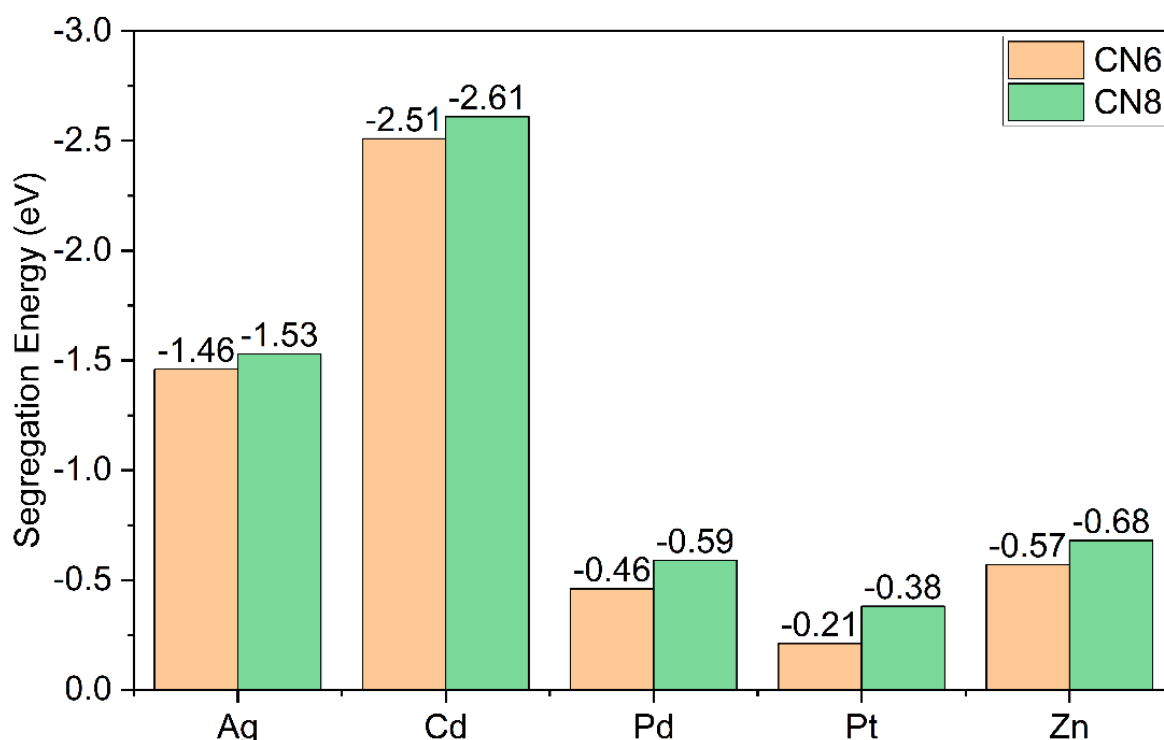


Figure 2. The segregation energy of the metal dopants Ag, Cd, Pd, Pt, and Zn in Cu_{54}M clusters. Dopant metal located at two different coordination sites: CN6 and CN8.

A descriptor to analyze the global reactivity descriptor is the gap energy $\Delta_{\text{H-L}}$, which relates to the energy cost for an electron to jump from the HOMO to the LUMO orbital. Therefore, $\Delta_{\text{H-L}}$ characterizes the chemical stability of the system, with a higher value corresponding to a more chemically stable (less reactive) cluster. The $\Delta_{\text{H-L}}$ for pure Cu_{55} atom is 0.028 eV, consistent with the literature value of 0.03 eV [55]. In Table 1 and Figure S1b of Supplementary Information, the single-doped atom clusters Cu_{54}Ag (CN6) and Cu_{54}Zn (CN6) show small $\Delta_{\text{H-L}}$ values of 1×10^{-4} and 5×10^{-4} eV, respectively. The single atom doped Cu_{54}Ag (CN8) and Cu_{54}Zn (CN8) show larger $\Delta_{\text{H-L}}$ values of 4.9×10^{-2} and 4.1×10^{-2} eV. This shows that the coordination environment of the metal dopant affects the gap energy $\Delta_{\text{H-L}}$ and, therefore, the reactivity of the cluster. Overall, the values of $\Delta_{\text{H-L}}$ are between 1×10^{-4} and 1.7×10^{-1} eV. The highest value of $\Delta_{\text{H-L}}$, 1.7×10^{-1} eV, is found for $\text{Cu}_{43}\text{Zn}_{12}$. The charge distribution in CuM clusters depends on the doping metal. This will influence CO_2 adsorption and subsequent CO_2 reduction because the electron transfer occurs from the electron-rich metal to the C atom, which in CO_2 is in its highest oxidation state. In the decorated clusters (Cu_{54}M , $\text{Cu}_{43}\text{M}_{12}$, and $\text{Cu}_{25}\text{M}_{30}$), when M is Ag, Pd or Pt, charge is transferred from Cu to M (negative ΔQ_{M}), and when M is Cd or Zn charge is transferred from M to Cu (positive ΔQ_{M}). In the core@shell $\text{Cu}_{13}\text{M}_{42}$ architecture, when M = Ag, Pd and Pt, the core is positively charged because of the charge transfer from Cu to M, while the shell has a negative charge. Vice versa for $\text{Cu}_{13}\text{M}_{42}$ with M = Cd and Zn. The effect of atomic radii, covalent radii, van-der radii, and electronegativity difference (ΔE_{N}) on bond lengths and surface area are discussed and available in Supplementary Information (Table S2). Regarding the surface energy, all clusters have negative γ values signifying the stability of the clusters compared to the bulk.

3.2. Adsorption and Activation of CO_2 on Cu and CuM Clusters

CO_2 is a linear molecule with two equivalent C–O bonds (length = 1.12 Å).¹³ Before its dissociation, the first step in the catalytic conversion of CO_2 is its adsorption on the catalyst surface. CO_2 can maintain the geometric properties of gas-phase CO_2 (physisorption) or become activated because of the charge transferred from the metal catalyst to the π^*

molecular orbitals of the CO₂ molecule (chemisorption) resulting in the elongation of the C–O bonds and decrease in the O–C–O bond angle (linear to bent mode) [56]. Here, we have conducted a detailed characterization of the adsorption and activation of CO₂ on the pure copper cluster Cu₅₅ and the copper-metal clusters, Cu₅₄M (CN6 and CN8), Cu₄₃M₁₂ (CN6), Cu₂₅M₃₀ (CN8) and Cu₁₃M₄₂ (core@shell), with M = Ag, Cd, Pd, Pt and Zn. These models can provide insights into the influence of surface chemistry on the activation of the CO₂ molecule. The structures of CO₂ on the CuM clusters are shown in Figure 3. The associated values of adsorption energies (E_{ads}), bond angles, bond elongations and Bader charges of CO₂ adsorbed on the CuM clusters are listed in Table 2. The adsorption energy was calculated as

$$E_{ads} = E_{CuM \cdots CO_2} - E_{CuM} - E_{CO_2} \quad (8)$$

where the first term is the total energy of the CuM⋯CO₂ system, and the second and third terms are the energies of the isolated cluster and CO₂ molecules, respectively. CO₂ is physisorbed on all Cu-Ag and core@shell clusters as indicated by the absence of significant deviations of the bond angle, bond elongation of adsorbed CO₂ from the gas-phase values, and small charge transfer between Cu and M ($\Delta Q_M \sim 0.04e$). In Figure 3 and Table 2, $\eta(Cu, C)$ and $\eta(M, C)$ refer to configurations in which the C atom of the CO₂ molecule is coordinated to the Cu and M atoms, respectively. In each chemisorbed state, there is a decrease in the O–C–O angle and an increase in charge transfer. In the single metal-doped systems, Cu₅₄M, at the CN6 active site, the coordination state $\eta(Cu, C)$ occurs for M = Cd and Zn and $\eta(M, C)$ occurs for M = Pd and Pt. In single metal-doped clusters at CN8, the $\eta(Cu, C)$ exists for M = Cd and $\eta(M, C)$ is present for M = Pd and Pt. Both $\eta(Cu, C)$ and $\eta(Zn, C)$ exist for Cu₅₄Zn on the CN8 active site. In the 12-atom doped Cu₄₃M₁₂ clusters, $\eta(Cu, C)$ is present for M = Cd, Zn and $\eta(M, C)$ exists in all systems except for Cu₄₃Ag₁₂. The 30-atom doped nano catalysts show the same trend as the 12-atom, except for the absence of $\eta(Cd, C)$ in Cu₄₃Cd₁₂. The $\eta(Cu, C)$ and $\eta(M, C)$ coordination do not exist in the core@shell models because CO₂ only physisorbs. In terms of adsorption energy, in the absence of $\eta(M, C)$, the physisorption energy of CO₂ always dominates. Similarly, in the absence of $\eta(Cu, C)$, the chemisorption energy of $\eta(M, C)$ configuration always dominates. When both $\eta(Cu, C)$ and $\eta(M, C)$ occur on a particular site, then again $\eta(Cu, C)$ is the most stable coordination mode.

	1-atom (CN6)		CN8		12-atom (CN6)		30-atom (CN8)		Core@Shell CN6 (CN8)	
	$\eta(Cu, C)$	$\eta(M, C)$	$\eta(Cu, C)$	$\eta(M, C)$	$\eta(Cu, C)$	$\eta(M, C)$	$\eta(Cu, C)$	$\eta(M, C)$	$\eta(M, C)$	$\eta(M, M)$
Ag										
	-0.20	-0.20	-0.18	-0.19	-0.21	-0.21	-0.22	-0.21	-0.23	-0.15
Cd										
	0.07	-0.18	0.14	-0.17	-0.44	-0.23	-0.09	-0.64	-0.58	-0.11
Pd										
	-0.20	-0.33	-0.18	-0.22	-0.22	-0.25	0.00	-0.52	-0.48	-0.13
Pt										
	-0.19	-0.56	-0.21	-0.43	-0.07	-0.34	-0.34	-0.56	-0.39	-0.10
Zn										
	-0.13	-0.20	0.05	0.26	-0.22	0.13	-0.50	-0.07	-0.37	-0.20

Figure 3. The structures and adsorption energies (in eV) of CO₂ on the CuM clusters.

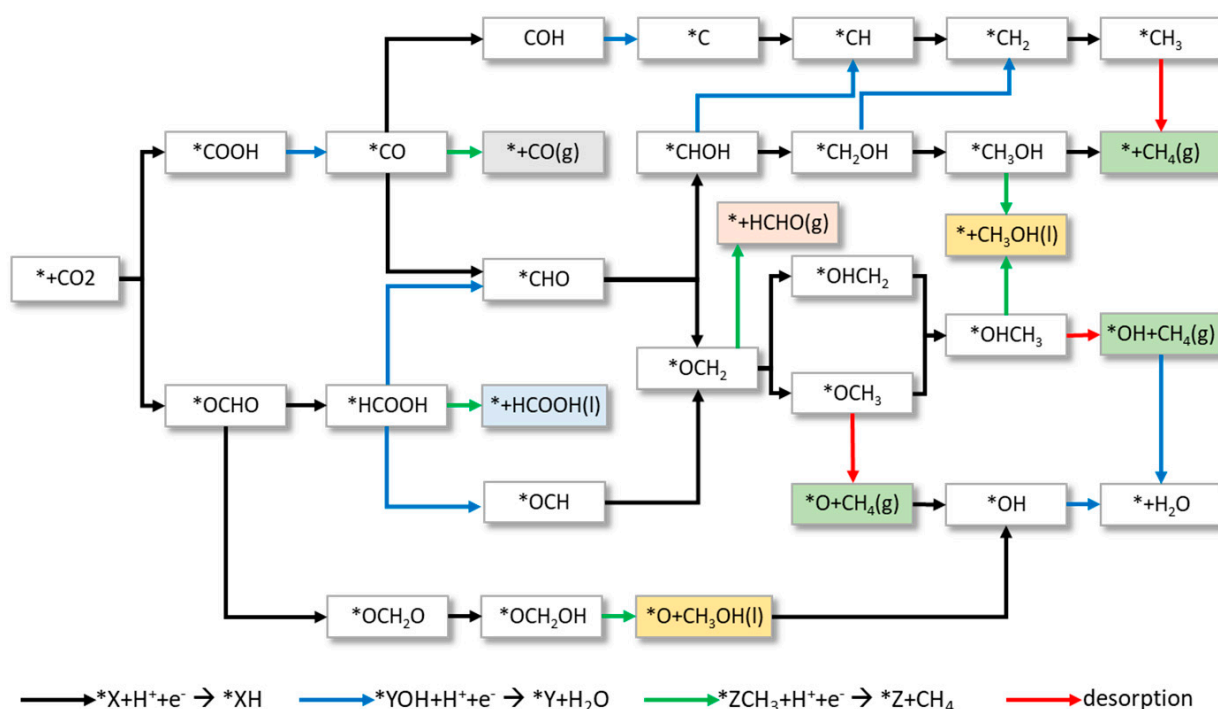
Table 2. The adsorption energies (E_{ads} , eV), bond angles (θ_{OCO} , °), charge difference (ΔQ_{M} , Coulomb) bond elongations (Δl_{CO} , Å) and d-bands center (δ_{d} , eV) of CO_2 adsorbed on the Cu-M nanoclusters ($\text{M} = \text{Ag}, \text{Cd}, \text{Pd}, \text{Pt}$ and Zn). The symbols $\eta(\text{Cu}, \text{C})$ and $\eta(\text{M}, \text{C})$ refer to the coordination of the C atom of the adsorbed CO_2 molecule to the Cu and M atoms, respectively.

	E_{ads}		$\theta(\text{O-C-O})$		ΔQ_{M}		Δl_{CO}	δ_{d}
	$\eta(\text{Cu}, \text{C})$	$\eta(\text{M}, \text{C})$	$\eta(\text{Cu}, \text{C})$	$\eta(\text{M}, \text{C})$	$\eta(\text{Cu}, \text{C})$	$\eta(\text{M}, \text{C})$		
Cu_{55}	−0.01	—	33.40	—	—	—	0.05	−2.27
1-atom doping (CN6)								
$\text{Cu}_{54}\text{Ag}_1$	−0.20	−0.20	0.340	0.460	0.04	0.04	0.00	−2.28
$\text{Cu}_{54}\text{Cd}_1$	0.07	−0.18	43.84	0.250	0.61	0.04	0.09	−2.38
$\text{Cu}_{54}\text{Pd}_1$	−0.20	−0.33	0.710	40.12	0.04	0.51	0.17	−2.29
$\text{Cu}_{54}\text{Pt}_1$	−0.19	−0.56	0.750	44.67	0.04	0.57	0.21	−2.29
$\text{Cu}_{54}\text{Zn}_1$	−0.13	−0.20	47.45	0.300	0.70	0.04	0.23	−2.36
1-atom doping (CN8)								
$\text{Cu}_{54}\text{Ag}_1$	−0.18	−0.19	0.65	0.42	0.04	0.04	0.00	−2.28
$\text{Cu}_{54}\text{Cd}_1$	0.14	−0.17	41.3	0.41	0.58	0.05	0.15	−2.34
$\text{Cu}_{54}\text{Pd}_1$	−0.18	−0.22	0.72	45.52	0.05	0.63	0.17	−2.28
$\text{Cu}_{54}\text{Pt}_1$	−0.21	−0.43	1.28	50.97	0.63	0.71	0.24	−2.26
$\text{Cu}_{54}\text{Zn}_1$	0.05	0.26	48.8	52.21	0.76	0.86	0.27	−2.34
12-atom doping (CN6)								
$\text{Cu}_{43}\text{Ag}_{12}$	−0.21	−0.21	0.660	0.300	0.04	0.04	0.01	−2.67
$\text{Cu}_{43}\text{Cd}_{12}$	−0.44	−0.23	48.50	45.60	0.75	0.68	0.23	−4.03
$\text{Cu}_{43}\text{Pd}_{12}$	−0.22	−0.25	0.470	38.02	0.04	0.49	0.19	−2.12
$\text{Cu}_{43}\text{Pt}_{12}$	−0.07	−0.34	1.260	42.38	0.78	0.53	0.29	−2.05
$\text{Cu}_{43}\text{Zn}_{12}$	−0.22	0.13	49.22	49.30	0.75	0.77	0.27	−3.72
30-atom doping (CN8)								
$\text{Cu}_{25}\text{Ag}_{30}$	−0.22	−0.23	0.490	0.620	0.04	0.04	0.00	−3.12
$\text{Cu}_{25}\text{Cd}_{30}$	−0.09	−0.64	32.19	0.240	0.65	0.05	0.27	−5.27
$\text{Cu}_{25}\text{Pd}_{30}$	0.00	−0.52	35.30	42.33	0.38	0.48	0.25	−1.49
$\text{Cu}_{25}\text{Pt}_{30}$	−0.34	−0.56	1.070	44.72	0.02	0.49	0.29	−1.75
$\text{Cu}_{25}\text{Zn}_{30}$	−0.50	−0.37	49.68	50.85	0.75	0.82	0.23	−4.61
42-atom doping (core@shell)								
$\text{Cu}_{13}\text{Ag}_{42}$	−0.15	−0.21	0.37	0.34	0.03	0.04	0.00	−3.56
$\text{Cu}_{13}\text{Cd}_{42}$	−0.11	−0.20	0.75	0.46	0.04	0.06	0.00	−7.29
$\text{Cu}_{13}\text{Pd}_{42}$	−0.13	−0.22	1.96	2.04	0.04	0.04	0.00	−1.58
$\text{Cu}_{13}\text{Pt}_{42}$	−0.10	−0.17	0.82	1.09	0.02	0.03	0.00	−1.92
$\text{Cu}_{13}\text{Zn}_{42}$	−0.20	−0.18	0.10	0.41	0.02	0.04	0.00	−6.23

3.3. Mechanism of CO_2 Reduction Reaction to C1 Products on Cu-M Clusters and Cu Surfaces

In this section, we present calculations of the mechanism of electrochemical CO_2 reduction. Scheme 1 shows the pathways and intermediates for the formation of the following C1 products: CO, HCOOH, CH_2O , CH_4 and CH_3OH . Depending on the atom coordinated to the catalyst, O or C, the first CPET step leads to two intermediates, $^*\text{OCHO}$ and $^*\text{COOH}$. The second CPET will determine whether the $2e^-$ products HCOOH or CO is formed. Subsequent CPET will lead to $4e^-$ (CH_2O), $6e^-$ (CH_3OH) and $8e^-$ (CH_4) C1 products. Compared to other catalytic reactions, the pathway of the eCO_2RR is more complex because of the number of intermediates involved. According to Equation 1, the

optimal reaction pathway is determined by the lowest free energy pathway at the applied potential U .



Scheme 1. Reaction pathways to the C1 products CO, HCOOH, CH₂O, CH₄ and CH₃OH.

3.3.1. Electrocatalytic CO₂ conversion to CO and HCOOH

We computed the free energy of reactions (ΔG) of the elementary steps to the CO₂ conversion to HCOOH and CO on the following systems: icosahedral Cu₅₅ cluster; decorated and core@shell Cu-M bimetallic clusters; Cu(100), Cu(110), Cu(111) and Cu(211) surfaces. In the context of the CHE model (see Equation 1), we define the potential limiting step (ΔG_{PLS}) as the elementary reaction in the eCO₂RR to CO or HCOOH (at $U = 0$ V) with the highest ΔG value (a high ΔG_{PLS} corresponds to poor catalytic performance). The elementary steps leading to the formation of CO are: (i) CO₂ adsorption ($CO_2 \rightarrow *CO_2$, ΔG_{*CO_2}); (ii) CPET to convert $*CO_2$ to C-coordinated formate ($*CO_2 + H^+ + e^- \rightarrow *COOH$, ΔG_{*COOH}); (iii) CPET to convert formate to adsorbed carbon monoxide ($*COOH + H^+ + e^- \rightarrow *CO + H_2O$, ΔG_{*CO}); (iv) the release, from the catalyst surface, of gas-phase CO ($*CO \rightarrow CO(g)$, ΔG_{CO}). The structures of the optimized $*COOH$ and $*CO$ on all Cu and CuM systems are reported in Supplementary Information (Figures S2–S8).

Pure copper: CO₂-to-CO conversion. The Gibbs free energy diagrams for the CO₂-to-CO conversion on the monometallic 55-atom cluster and the (100), (110), (111) and (211) surfaces are reported in Figure 4a. There is a significant dependence of the stability of the $*COOH$ and $*CO$ intermediates on the surface morphology and coordination environment. The (211) facet has better catalytic performance (lower ΔG_{PLS}) towards CO formation than any other surfaces but higher than Cu₅₅. This cluster was, therefore, taken as the reference system to assess the performance of the bimetallic clusters. The competitive HER ($H^+ + e^- \rightarrow \frac{1}{2} H_2$) in Figure 4b shows a similar morphology dependence: unfavourable on the (110) surface; highly favorable on the (100) surface; moderately favorable on the (211) surface and the Cu₅₅ cluster.

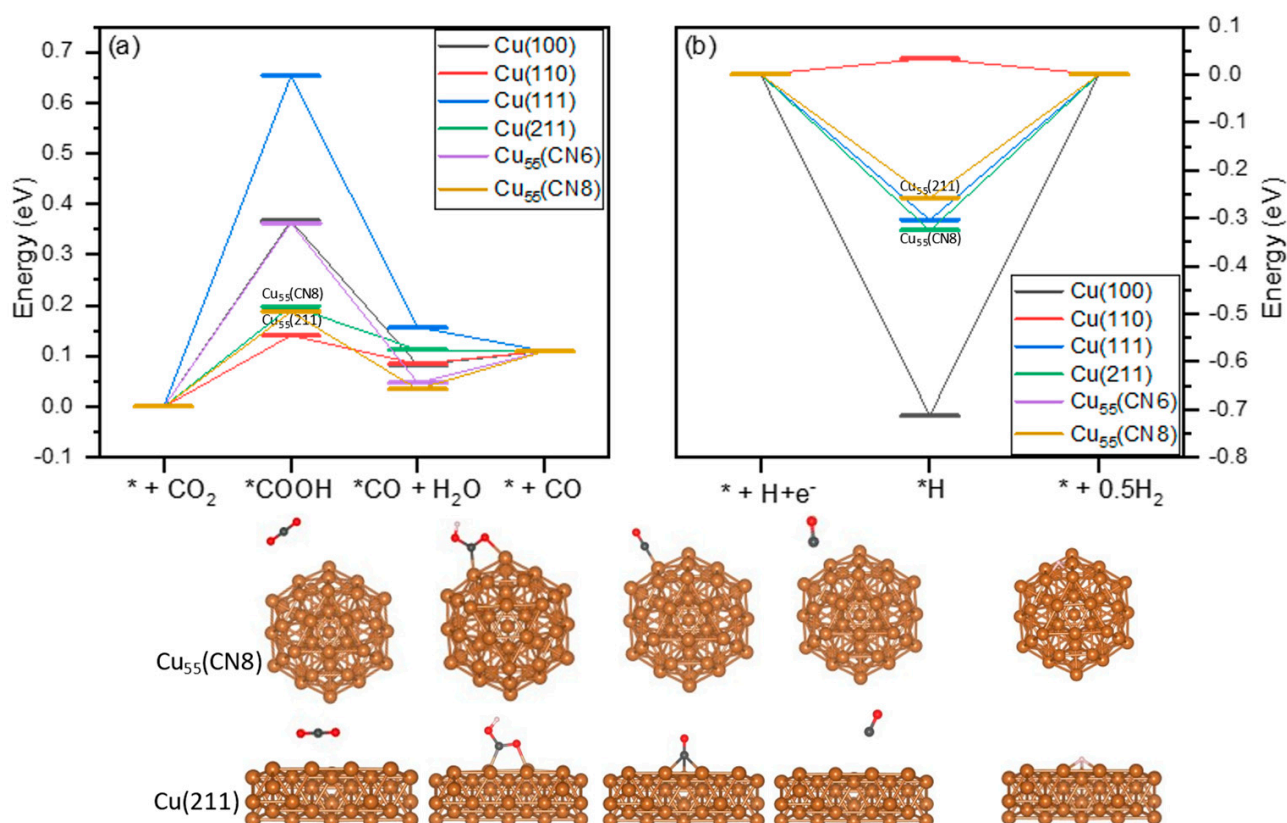


Figure 4. The Gibbs free energy diagram for the (a) CO₂ reduction reaction to CO and the (b) hydrogen evolution reaction on Cu₅₅ cluster and on the (100), (110) and (111) Cu surfaces.

Bimetallic clusters: CO₂-to-CO conversion. The free energy diagrams for the eCO₂RR to CO and the HER on CuM are reported in Figure 5. In the single metal doped clusters, Cu₅₄M, the value of ΔG_{PLS} depends on both the coordination site and nature of the metal. The ΔG_{PLS} is lower when the reaction occurs on CN6 for M equal to Cd (0.16 eV), Pd (0.23 eV) and Pt (0.53 eV) compared to CN8, Cd (0.12 eV), Pd (0.42 eV) and Pt (0.78 eV). However, for Ag (0.27 eV) and Zn (0.18 eV), CN6 shows higher ΔG_{PLS} than CN8, Ag (0.14 eV) and Zn (0.14 eV). Each intermediate shows strong chemisorption with a low ΔG_{PLS} value and vice versa. For both CN6 and CN8 systems, HER is dominant (lower ΔG_H) over eCO₂RR because of the strong CO binding to the cluster, leading to a large ΔG_{*CO} ; the exception is M = Pt. When the number of metal dopants on the CuM cluster increases, Cu₄₃M₁₂, so does the value of ΔG_{PLS} : Ag (0.24 eV), Pd (0.32 eV), Pt (0.86 eV) and Zn (0.19 eV). The exception is Cd (0.25 eV). The CO generation remains dominant over HER, except again for Pt, for the same reasons discussed for the single atom doped clusters. With further increase in the doping and change in surface chemistry in the Cu₂₅M₃₀ clusters, the HER becomes more favorable with a small value of $|\Delta G_H|$ for Ag (0.10 eV), Cd (0.19 eV), Pd (0.92 eV) and Pt (0.76 eV) compared to the ΔG_{PLS} of the eCO₂RR of Ag (0.37 eV), Cd (0.29 eV), Pd (1.61 eV) and Pt (1.23 eV). At this doping concentration, only Zn, with $\Delta G_{PLS} = 0.40$ eV and $\Delta G_H = 0.49$ eV, favors eCO₂RR over HER. All core@shell models are more active towards HER than eCO₂RR: the ΔG_H values of Ag (0.07 eV), Cd (0.45 eV), Pd (−0.62 eV), Pt (−0.59 eV) and Zn (−0.27 eV) are lower than the ΔG_{PLS} values of Ag (0.76 eV), Cd (0.91 eV), Pd (1.12 eV), Pt (1.09 eV), and Zn (0.58 eV).

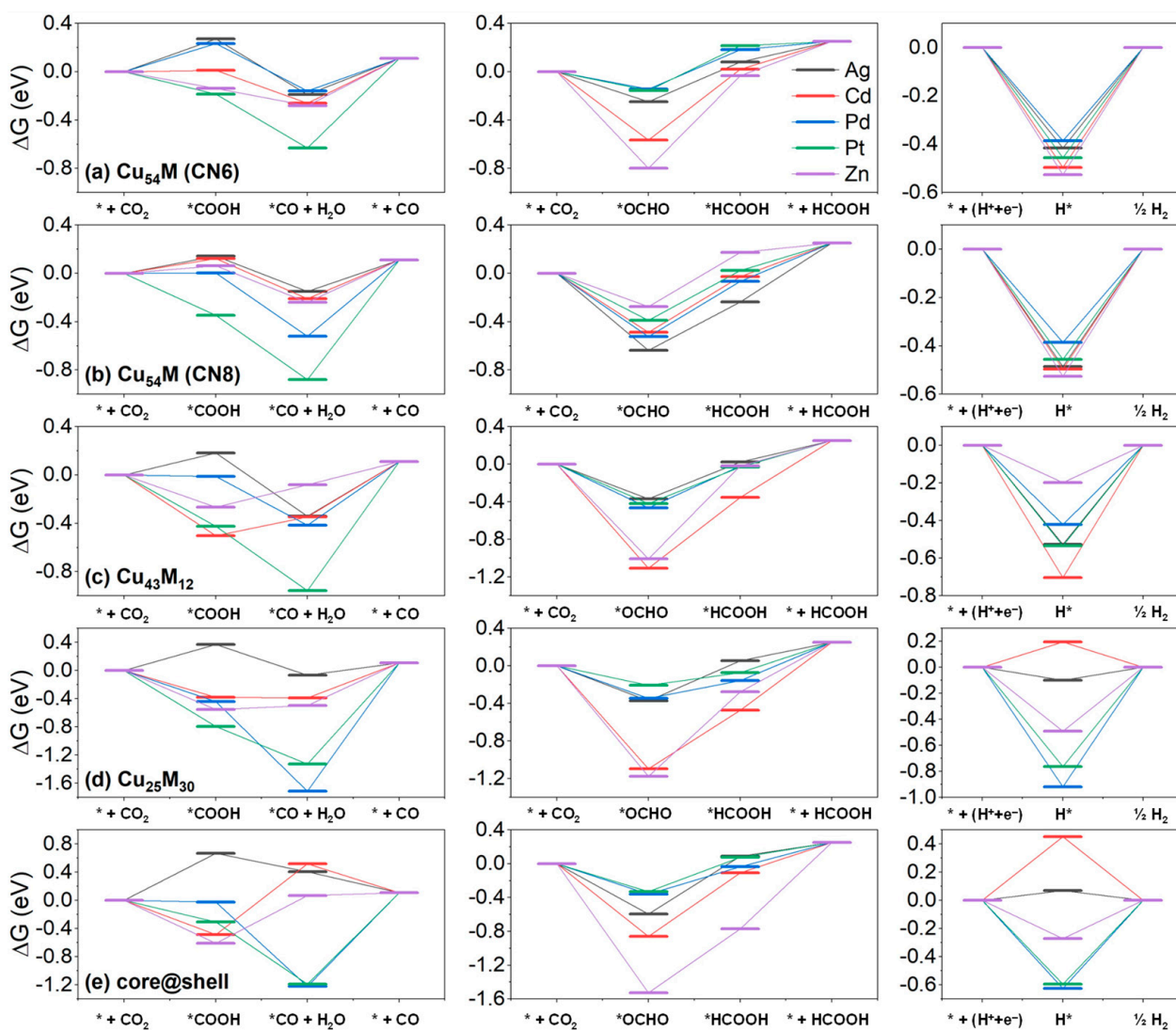


Figure 5. The Gibbs free energy diagram for the CO₂ reduction to CO (left), CO₂ reduction to HCOOH (centre), and hydrogen evolution reaction (right) on the CuM clusters (M = Ag, Cd, Pd, Pt and Zn): (a) Cu₅₄M with CN6, (b) Cu₅₄M with CN8, (c) Cu₄₃M₁₂, (d) Cu₂₅M₃₀ and (e) core@shell.

Bimetallic clusters: CO₂-to-HCOOH conversion. For HCOOH formation, the steps are the CPET to convert adsorbed *CO₂ to O-coordinated formate (*CO₂ + H⁺ + e[−] → *OCO_H, ΔG_{*OCO_H}) and the CPET to convert adsorbed formate to liquid phase formic acid (*OCHO + H⁺ + e[−] → HCOOH(l), ΔG_{HCOOH}). In Figure 5, the ΔG_{PLS} value for HCOOH of Cu₅₄M with CN6 for Ag (0.33 eV), Pd (0.33 eV) and Pt (0.37 eV) in the CuM cluster with CN8 for Ag (0.46 eV), Cd (0.46 eV), Pt (0.45 eV), Cu₄₃M₁₂ with Ag (0.39 eV), Pt (0.39 eV), Cu₂₅M₃₀ with Pd (0.19 eV), Pt (0.13 eV) and finally core@shell with Pd (0.33 eV), Pt (0.41 eV) are dominant over HER. We can explain this behaviour by considering the value of the d-band center (Table 2), which decreases for Ag, Cd and Zn with increasing doping concentration. The adsorption energy of the intermediates involved in the CO or HCOOH reaction pathway also decreases. Similarly, the higher position of the d-band center for Pd and Pt leads to an increase in the intermediate adsorption energy. Therefore, the core@shell model with low d-band center, Ag (−3.56 eV), Cd (−7.29 eV) and Zn (−6.23 eV), show poor catalytic performance, and Pd (−1.58 eV) and Pt (−1.92 eV) show good catalytic performance for HCOOH. Overall, the core@shell promotes the formation of HCOOH, and single metal-doped clusters show good catalytic performance for CO, except for Pt, which catalyzes HCOOH formation.

3.3.2. Electrocatalytic CO₂ conversion to CH₂O, CH₃OH, and CH₄

The free energy diagrams for the eCO₂RR to formaldehyde (CH₂O), methanol (CH₃OH) and methane (CH₄) on the CuM clusters are reported in Figure 6.

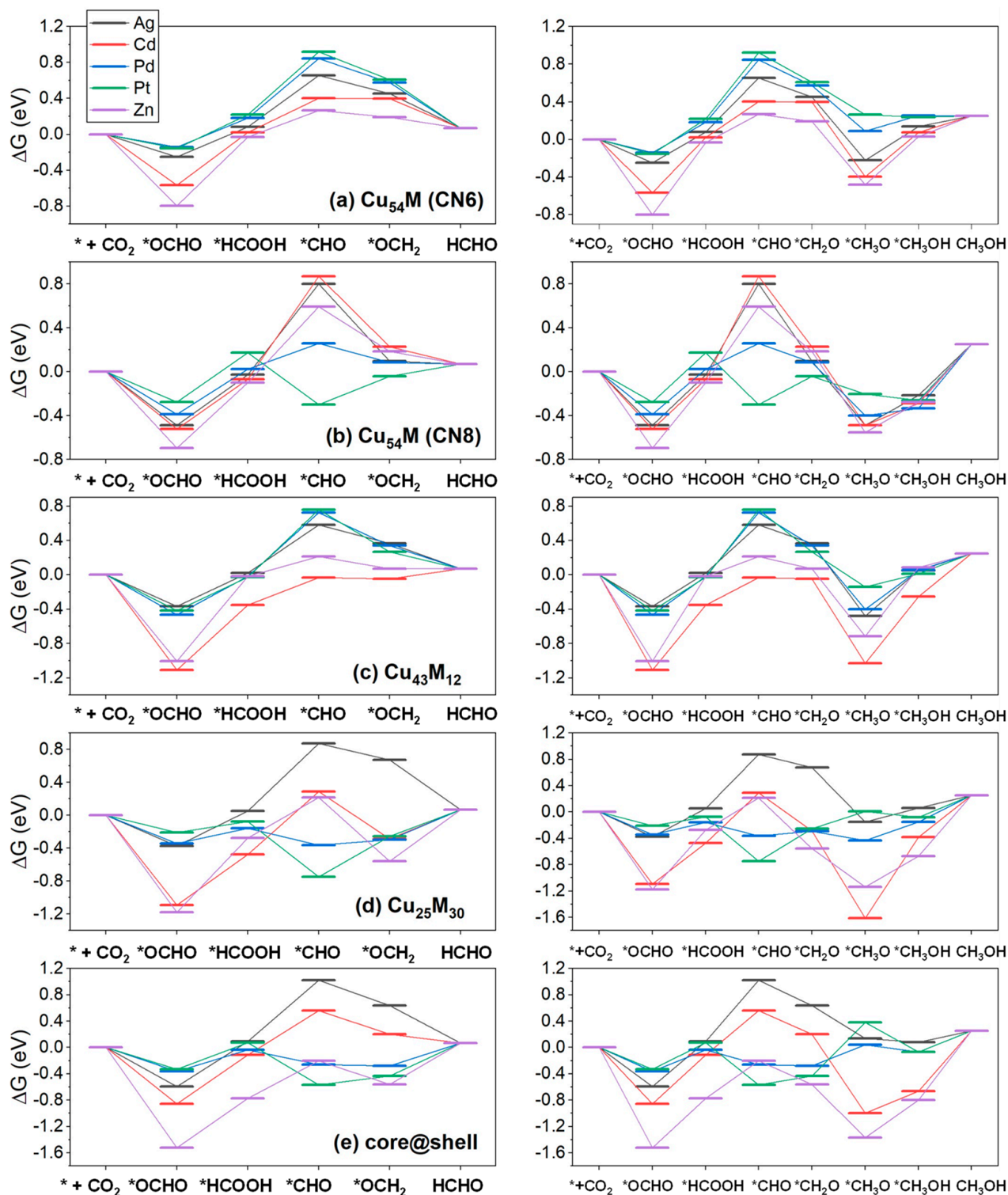


Figure 6. The Gibbs free energy diagram for the eCO₂RR pathways to HCHO (left) and CH₃OH (right) on the CuM clusters (M = Ag, Cd, Pd, Pt and Zn): (a) Cu₅₄M with CN6, (b) Cu₅₄M with CN8, (c) Cu₄₃M₁₂, (d) Cu₂₅M₃₀ and (e) core@shell.

Bimetallic clusters: CH₂O formation. After the eCO₂RR reduction to *CO or *HCOOH, further CPET steps generates three distinct intermediates: *CHO, *COH or *OCH. Among them, *CHO is the easiest to generate, as illustrated by the free energy diagram for the formation of these species, where the lowest ΔG_{PLS} is for COH. A subsequent CPET step leads to the formation of formaldehyde: $*\text{CHO} + \text{H}^+ + \text{e}^- \rightarrow *\text{OCH}_2 \rightarrow * + \text{CH}_2\text{O}(\text{g})$. Due to the stronger O-affinity, CH₂O prefers *OCHO than the *COOH route. CH₂O generation shows lowest ΔG_{PLS} values on Cu₂₅Pd₃₀ (0.19 eV) and core@shell Cu@Pd (0.33 eV). As the ΔG_{H} values on Cu₂₅Pd₃₀ (0.92 eV) and core@shell Cu@Pd (0.62 eV) are higher than ΔG_{PLS} values, the CO₂ conversion to CH₂O is dominant over HER on these clusters. CuPd is also favorable towards CH₂O formation as the ΔG_{PLS} values are higher than ΔG_{H} on these clusters. The values of ΔG_{PLS} are 0.45 eV for Cu₅₄Pt (CN8), 0.49 eV for Cu₂₅Pt₃₀, and 0.44 eV for the Cu₅₄Pt (CN8) and the core@shell Cu₂₅Pt₃₀ clusters. In comparison, the ΔG_{H} values on Cu₅₄Pt (CN8), Cu₂₅Pt₃₀ and Cu@Pt are 0.46 eV, 0.76 eV and 0.59 eV, respectively. The Gibbs free energy diagram of the eCO₂RR to CH₂O on these systems is given as Figure 6a–e

Bimetallic clusters: CH₃OH formation. The formation of CH₃OH involves five CPET steps. The first three reduction steps coincide to the eCO₂RR to CH₂O. The *CHO is reduced to *CHOH or *OCH₂ depending on if the O or C atoms are protonated. This leads to four possible routes to convert CO₂ to CH₃OH:

1. $*\text{COOH} \rightarrow *\text{CO} \rightarrow *\text{CHO} \rightarrow *\text{OCH}_2 \rightarrow *\text{OCH}_3 \rightarrow *\text{OHCH}_3$;
2. $*\text{OCHO} \rightarrow *\text{OCH}_2\text{O} \rightarrow *\text{OCH}_2\text{OH} \rightarrow *\text{O} + \text{CH}_3\text{OH} \rightarrow *\text{OH} \rightarrow * + \text{H}_2\text{O}$;
3. $*\text{OCHO} \rightarrow *\text{HCOOH} \rightarrow *\text{CHO} \rightarrow *\text{CHOH} \rightarrow *\text{CH}_2\text{OH} \rightarrow *\text{OHCH}_3$;
4. $*\text{OCHO} \rightarrow *\text{HCOOH} \rightarrow *\text{CHO} \rightarrow *\text{OCH}_2 \rightarrow *\text{OHCH}_2 \rightarrow *\text{OHCH}_3$.

Out of these four paths, our calculations predict the last one as the most suitable for CH₃OH formation. Similar to CH₂O, the Cu₂₅Pd₃₀ and core@shell Cu@Pd show the lowest ΔG_{PLS} , 0.28 eV and 0.33 eV, respectively, and still, these reactions are dominant over HER.

Bimetallic clusters: CH₄ formation. The main 8-electron product of eCO₂RR is CH₄, involving eight CPET transfer steps. It follows five different reaction pathways:

1. $*\text{CHO} \rightarrow *\text{CHOH} \rightarrow *\text{CH} \rightarrow *\text{CH}_2 \rightarrow *\text{CH}_3 \rightarrow * + \text{CH}_4$;
2. $*\text{CHO} \rightarrow *\text{CHOH} \rightarrow *\text{CH}_2\text{OH} \rightarrow *\text{CH}_2 \rightarrow *\text{CH}_3 \rightarrow * + \text{CH}_4$;
3. $*\text{CHO} \rightarrow *\text{OCH}_2 \rightarrow *\text{OHCH}_2 \rightarrow *\text{OHCH}_3 \rightarrow *\text{OH} + \text{CH}_4 \rightarrow * + \text{H}_2\text{O}$;
4. $*\text{CHO} \rightarrow *\text{OCH}_2 \rightarrow *\text{OCH}_3 \rightarrow *\text{OHCH}_3 \rightarrow *\text{OH} + \text{CH}_4 \rightarrow * + \text{H}_2\text{O}$;
5. $*\text{CHO} \rightarrow *\text{OCH}_2 \rightarrow *\text{OCH}_3 \rightarrow *\text{O} + \text{CH}_4 \rightarrow *\text{OH} \rightarrow * + \text{H}_2\text{O}$.

The free energy diagrams along these pathways are given in Figures S9 and S10 of Supplementary Information.

Competition between CH₄ and H₂ formation. HER is a competitive reaction in eCO₂RR and can reduce the efficiency of the eCO₂RR reaction leading to poor selectivity of the catalyst. To evaluate the selectivity of eCO₂RR vs. HER, we have reported in Figure 7 the limiting potential difference $\Delta\Delta G_{\text{PLS}} = \Delta G_{\text{PLS}}(\text{eCO}_2\text{RR}) - \Delta G_{\text{H}}(\text{HER})$ for the five reaction pathways leading to the formation of CH₄ on the CuM clusters. The higher the (positive) value of $\Delta\Delta G_{\text{PLS}}$, the higher the selectivity for CH₄. Only CuPd shows good catalytic performance towards CH₄ formation. Through the reaction pathway (1), Cu₂₅Pd₃₀ has a positive $\Delta\Delta G_{\text{PLS}}$. The Cu₄₃Ag₁₂ and Cu₄₃Cd₁₂ clusters show a small negative $\Delta\Delta G_{\text{PLS}}$ value. For pathways (2) and (3), the Cu₂₅Pd₃₀ and Cu@Pd show a positive $\Delta\Delta G_{\text{PLS}}$ value and hence these two systems are selective towards CH₄. Like pathway (1), the Cu₄₃Ag₁₂ and Cu₄₃Cd₁₂ show a very small $\Delta\Delta G_{\text{PLS}}$ for (2) which makes them also good candidates for catalyzing CH₄ formation. Finally, Cu₁₃Cd₄₂ shows a small $\Delta\Delta G_{\text{PLS}}$, which can be explained based on the d-band center and coordination environment: at the same doping concentration (1-atom) with CN6 and CN8, the 1-atom at CN6 show significantly low overpotential for all pathways leading to CH₄ generation. Single-doped clusters with CN6 and CN8 have similar d-band center values (Table 2), only the coordination environment is different, which means that the CN environment has a significant impact on the catalytic performance. Furthermore, the d-band center value increases with an increase in doping

concentration for Cu-Pd and Cu-Pt catalysts. Consequently, there is strong adsorption of the intermediates involved in the reaction (pathways 1 to 5). However, with $M = \text{Ag, Cd}$ and Zn , the values of d-band centers decreases, which leads to weak adsorption of the intermediates and poor catalytic performance towards CH_4 formation.

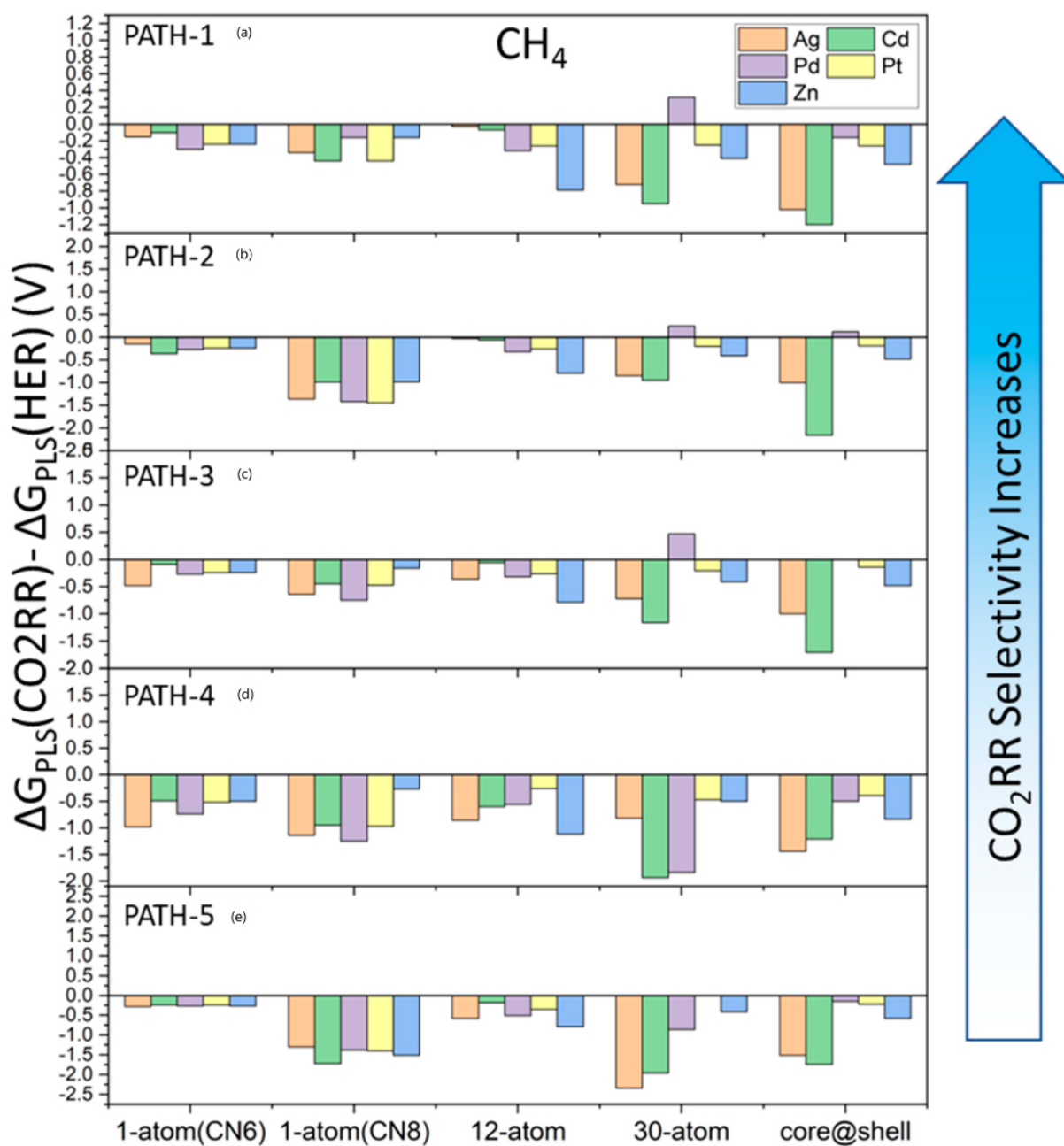


Figure 7. The limiting potential difference (ΔG_{PLS}) between CO_2RR to CH_4 and HER on the bimetallic CuM clusters ($M = \text{Ag, Cd, Pd, Pt}$ and Zn): (a) Cu_{54}M with CN6, (b) Cu_{54}M with CN8, (c) $\text{Cu}_{43}\text{M}_{12}$, (d) $\text{Cu}_{25}\text{M}_{30}$ and (e) core@shell.

3.3.3. Selectivity

The overpotentials (η) to C1 products for all CuM systems, summarized in Figure 8, were computed from the equilibrium (U_{eq}) and limiting (U_{L}) potentials (Figures 5 and 6). The values of U_{eq} for CO , HCOOH , CH_2O , CH_3OH and CH_4 are 0.12 V, 0.25 V, 0.07 V, 0.02 V and 0.17 V, respectively. For the Cu clusters doped with Ag, Cd and Zn, an increase in metal doping, particularly after 30-atom, leads to the HER becoming dominant over other

C1 products. This behaviour is clearly noticeable for the single atom doped clusters, Cu_{54}M with $\text{M} = \text{Ag}, \text{Cd}$ and Zn , which shows higher η values for HER than the corresponding core@shell systems. The values of the overpotential also show that a single atom doped system supports either CO or HCOOH. Therefore, small doping does not promote CH_3OH or CH_4 formation. As metal doping increases, the Cu-Pd and Cu-Pt clusters show lower overpotential for CH_2O , CH_3OH and CH_4 . Only $\text{Cu}_{25}\text{Pt}_{30}$ and $\text{Cu}_{13}\text{Pd}_{42}$ have the lowest overpotential for CH_4 .

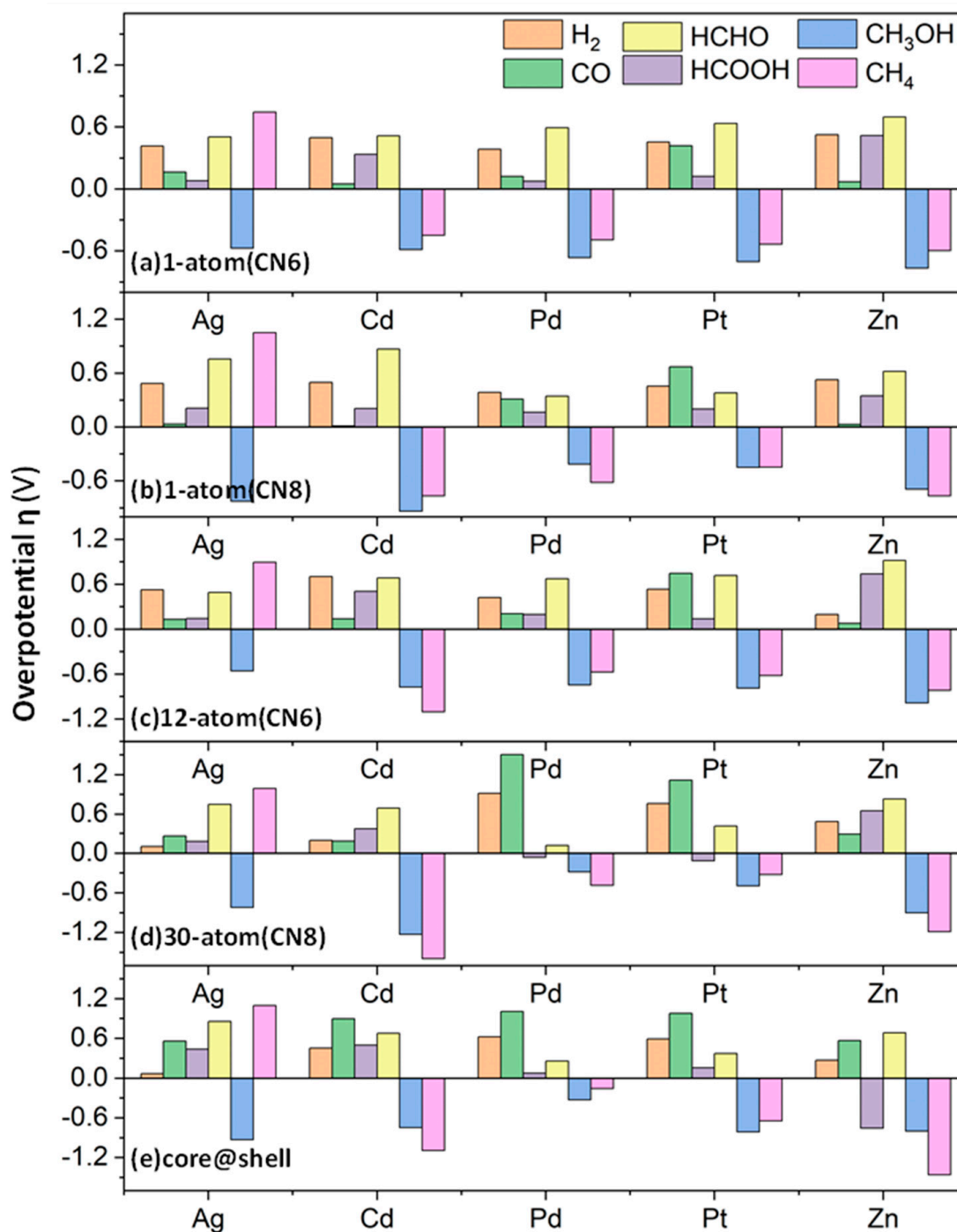


Figure 8. The overpotentials (η) for the electrocatalytic formation of H_2 , CO, HCOOH, CH_2O , CH_3OH and CH_4 on the CuM clusters ($\text{M} = \text{Ag}, \text{Cd}, \text{Pd}, \text{Pt}$ and Zn): (a) Cu_{54}M with CN6, (b) Cu_{54}M with CN8, (c) $\text{Cu}_{43}\text{M}_{12}$, (d) $\text{Cu}_{25}\text{M}_{30}$ and (e) core@shell.

4. Conclusions

In this work, the catalytic properties towards the electrochemical CO₂ reduction reaction of a series of icosahedral 55-atom Cu-based clusters doped with Ag, Cd, Pd, Pt and Zn were investigated using density functional theory calculations. The adsorption and activation of CO₂ on these clusters and all possible reaction paths that lead to the CO₂ reduction to C1 products (CO, HCOOH, CH₂O, CH₃OH and CH₄) were considered. Apart from the composition effects, the role of the coordination environment of the metal dopant on the catalytic performance of copper-based clusters was also investigated, with the results showing that nanoclusters with eight-coordinated metal dopants have better catalytic activity towards CO₂ activation. Single-atom doping with Cd and Zn is the best candidate for the CO₂-to-CO conversion, while core@shell with Ag, Pd and Pt is a good choice for formic acid or formaldehyde formation. The CuPt and CuPd systems show the lowest overpotential for methane formation. This work identifies the influence of size, metal coupling and metal coordination on CO₂ activation and intermediate stability and, consequently, the structure-property relationship in Cu-based mono and bi-metallic clusters for the selective CO₂ conversion to value-added C1 products.

Supplementary Materials: The following supporting information can be downloaded at: <https://www.mdpi.com/article/10.3390/nano13010087/s1>, Table S1: The energies (E), zero-point energies (ZPE), and entropies (S) of H₂(g), CO₂(g) and CO(g), and H₂O; Table S2: The atomic, covalent and Van der Waals radii, the electronegativity difference, electronic configuration, and calculated value of segregation energies (in eV) [57,58]; Figure S1: (a) The binding energy and (b) HOMO-LUMO (H-L) gap of Cu-M clusters with increasing doping concentration; Figure S2: The structure and adsorption energies (in eV) of COOH adsorbed on the Cu-M clusters; Figure S3: The structure and adsorption energies (in eV) of CO adsorbed on the Cu₅₄M clusters with CN6 and CN8 nano-catalysts; Figure S4: The structure and adsorption energies (in eV) of CO on the Cu₄₃M₁₂ and Cu₂₅M₃₀ clusters; Figure S5: The structure and adsorption energies (in eV) of CO on the Cu₄₃M₁₂ and Cu₂₅M₃₀ clusters; Figure S6: The structure and adsorption energies of H adsorbed on the Cu₄₃M₁₂ and Cu₂₅M₃₀ clusters at the Top, Hollow and Bridge positions; Figure S7: The structure and adsorption energies of H adsorbed on the Cu₄₃M₁₂ and Cu₂₅M₃₀ clusters at Top, Hollow and Bridge positions; Figure S8: The structures and adsorption energies of H adsorbed on the core@shell clusters at Top, Hollow and Bridge positions; Figure S9. Gibbs free energy diagram for the CH₄ formation on CuM clusters along pathways 1 to 5; Figure S10. Gibbs free energy diagram for CHO (a) and COH (b) formation on CuM clusters.

Author Contributions: Conceptualization of work: A.G.N. and D.D.T.; Conducting of experiments: A.G.N.; Computation: A.G.N.; Data analyses: A.G.N., A.-u.-R., A.H. and D.D.T.; Data dissemination & graphics: A.G.N., A.H. and D.D.T.; Writing of manuscript: A.G.N., A.-u.-R., G.A.C., D.D.T.; Project support: G.A.C., D.D.T. All authors have read and agreed to the published version of the manuscript.

Funding: A.G.N. acknowledges the Pakistan HEC-QMUL PhD Scholarships for funding. D.D.T. and G.A.C. acknowledged the ACT programme (Accelerating CCS Technologies, Horizon2020 Project No 299668), which funded the FUNMIN project. Financial contributions made from Department for Business, Energy & Industrial Strategy (BEIS) together with extra funding from NERC and EPSRC research councils, United Kingdom, ADEME (FR), MINECO-AEI (ES). We are grateful to the UK Materials and Molecular Modelling Hub for computational resources, which is partially funded by EPSRC (EP/P020194/1). We are grateful to the UK Materials and Molecular Modelling Hub for computational resources, which is partially funded by EPSRC (EP/P020194/1). Via our membership of the UK's HEC Materials Chemistry Consortium, which is funded by EPSRC (EP/L000202), this work used the ARCHER UK National Supercomputing Service.

Data Availability Statement: The data presented in this study are available on request from the corresponding author.

Acknowledgments: This research utilized Queen Mary's Apocrita HPC facility, supported by QMUL Research-IT. <http://doi.org/10.5281/zenodo.438045>, accessed on 16 December 2022.

Conflicts of Interest: The authors declare no conflict of interest.

References

1. IPCC. *Climate Change 2022: Mitigation of Climate Change*; Working Group III Report; Cambridge University Press: Cambridge, UK, 2022; p. 1454.
2. IPCC. *Climate Change and Land: An IPCC Special Report on Climate Change, Desertification, Land Degradation, Sustainable Land Management, Food Security, and Greenhouse Gas Fluxes in Terrestrial Ecosystems*; Shukla, P.R., Skea, J., Calvo Buendia, E., Masson-Delmotte, V., Pörtner, H.-O., Roberts, D.C., Zhai, P., Slade, R., Connors, S., van Diemen, R., et al., Eds.; Cambridge University Press: Cambridge, UK, 2019.
3. Bushuyev, O.S.; de Luna, P.; Dinh, C.T.; Tao, L.; Saur, G.; van de Lagemaat, J.; Kelley, S.O.; Sargent, E.H. What Should We Make with CO₂ and How Can We Make It? *Joule* **2018**, *2*, 825–832. [\[CrossRef\]](#)
4. Zhang, W.; Hu, Y.; Ma, L.; Zhu, G.; Wang, Y.; Xue, X.; Chen, R.; Yang, S.; Jin, Z. Progress and Perspective of Electrocatalytic CO₂ Reduction for Renewable Carbonaceous Fuels and Chemicals. *Adv. Sci.* **2018**, *5*, 1700275. [\[CrossRef\]](#) [\[PubMed\]](#)
5. Bagger, A.; Ju, W.; Varela, A.S.; Strasser, P.; Rossmeisl, J. Electrochemical CO₂ Reduction: A Classification Problem. *ChemPhysChem* **2017**, *18*, 3266–3273. [\[CrossRef\]](#) [\[PubMed\]](#)
6. Peterson, A.A.; Nørskov, J.K. Activity descriptors for CO₂ electroreduction to methane on transition-metal catalysts. *J. Phys. Chem. Lett.* **2012**, *3*, 251–258. [\[CrossRef\]](#)
7. Wu, J.; Huang, Y.; Ye, W.; Li, Y. CO₂ Reduction: From the Electrochemical to Photochemical Approach. *Adv. Sci.* **2017**, *4*, 1700194. [\[CrossRef\]](#)
8. He, Z.; Qian, Q.; Ma, J.; Meng, Q.; Zhou, H.; Song, J.; Liu, Z.; Han, B. Water-Enhanced Synthesis of Higher Alcohols from CO₂ Hydrogenation over a Pt/Co₃O₄ Catalyst under Milder Conditions. *Angew. Chemie Int. Ed.* **2016**, *55*, 737–741. [\[CrossRef\]](#)
9. Zhang, X.; Li, X.; Zhang, D.; Su, N.Q.; Yang, W.; Everitt, H.O.; Liu, J. Product selectivity in plasmonic photocatalysis for carbon dioxide hydrogenation. *Nat. Commun.* **2017**, *8*, 14542. [\[CrossRef\]](#)
10. Park, S.; Bézier, D.; Brookhart, M. An Efficient Iridium Catalyst for Reduction of Carbon Dioxide to Methane with Trialkylsilanes. *J. Am. Chem. Soc.* **2012**, *134*, 11404–11407. [\[CrossRef\]](#)
11. Klinkova, A.; de Luna, P.; Dinh, C.-T.; Voznyy, O.; Larin, E.M.; Kumacheva, E.; Sargent, E.H. Rational Design of Efficient Palladium Catalysts for Electroreduction of Carbon Dioxide to Formate. *ACS Catal.* **2016**, *6*, 8115–8120. [\[CrossRef\]](#)
12. Zhu, W.; Michalsky, R.; Metin, Ö.; Lv, H.; Guo, S.; Wright, C.J.; Sun, X.; Peterson, A.A.; Sun, S. Monodisperse Au Nanoparticles for Selective Electrocatalytic Reduction of CO₂ to CO. *J. Am. Chem. Soc.* **2013**, *135*, 16833–16836. [\[CrossRef\]](#)
13. Xie, H.; Wang, T.; Liang, J.; Li, Q.; Sun, S. Cu-based nanocatalysts for electrochemical reduction of CO₂. *Nano Today* **2018**, *21*, 41–54. [\[CrossRef\]](#)
14. Dickinson, H.L.A.; Symes, M.D. Recent progress in CO₂ reduction using bimetallic electrodes containing copper. *Electrochem. Commun.* **2022**, *135*, 107212. [\[CrossRef\]](#)
15. Kitchin, J.R.; Nørskov, J.K.; Barteau, M.A.; Chen, J.G. Role of Strain and Ligand Effects in the Modification of the Electronic and Chemical Properties of Bimetallic Surfaces. *Phys. Rev. Lett.* **2004**, *93*, 156801. [\[CrossRef\]](#) [\[PubMed\]](#)
16. Sinfelt, J.H.; Carter, J.L.; Yates, D.J.C. Catalytic hydrogenolysis and dehydrogenation over copper-nickel alloys. *J. Catal.* **1972**, *24*, 283–296. [\[CrossRef\]](#)
17. Shen, S.; He, J.; Peng, X.; Xi, W.; Zhang, L.; Xi, D.; Wang, L.; Liu, X.; Luo, J. Stepped surface-rich copper fiber felt as an efficient electrocatalyst for the CO₂RR to formate. *J. Mater. Chem. A* **2018**, *6*, 18960–18966. [\[CrossRef\]](#)
18. Hori, Y.; Takahashi, I.; Koga, O.; Hoshi, N. Selective formation of C₂ compounds from electrochemical reduction of CO₂ at a series of copper single crystal electrodes. *J. Phys. Chem. B* **2002**, *106*, 15–17. [\[CrossRef\]](#)
19. Sreejyothi, P.; Mandal, S.K. From CO₂ activation to catalytic reduction: A metal-free approach. *Chem. Sci.* **2020**, *11*, 10571–10593.
20. Higham, M.D.; Quesne, M.G.; Catlow, C.R.A. Mechanism of CO₂ conversion to methanol over Cu(110) and Cu(100) surfaces. *Dalt. Trans.* **2020**, *49*, 8478–8497. [\[CrossRef\]](#)
21. Studt, F.; Behrens, M.; Kunkes, E.L.; Thomas, N.; Zander, S.; Tarasov, A.; Schumann, J.; Frei, E.; Varley, J.B.; Abild-Pedersen, F.; et al. The Mechanism of CO and CO₂ Hydrogenation to Methanol over Cu-Based Catalysts. *ChemCatChem* **2015**, *7*, 1105–1111. [\[CrossRef\]](#)
22. Fajin, J.L.C.; Cordeiro, M.N.D.S.; Illas, F.; Gomes, J.R.B. Influence of step sites in the molecular mechanism of the water gas shift reaction catalyzed by copper. *J. Catal.* **2009**, *268*, 131–141. [\[CrossRef\]](#)
23. Behrens, M.; Studt, F.; Kasatkin, I.; Köhl, S.; Hävecker, M.; Abild-Pedersen, F.; Zander, S.; Girsdsies, F.; Kurr, P.; Knierp, B.; et al. The active site of methanol synthesis over Cu/ZnO/Al₂O₃ industrial catalysts. *Science* **2012**, *759*, 893–898. [\[CrossRef\]](#)
24. Hori, Y.; Takahashi, I.; Koga, O.; Hoshi, N. Electrochemical reduction of carbon dioxide at various series of copper single crystal electrodes. *J. Mol. Catal. A Chem.* **2003**, *199*, 39–47. [\[CrossRef\]](#)
25. Li, Q.; Zhang, Y.; Shi, L.; Wu, M.; Ouyang, Y.; Wang, J. Dynamic structure change of Cu nanoparticles on carbon supports for CO₂ electro-reduction toward multicarbon products. *InfoMat* **2021**, *3*, 1285–1294. [\[CrossRef\]](#)
26. Steinhauer, B.; Kasireddy, M.R.; Radnik, J.; Martin, A. Development of Ni-Pd bimetallic catalysts for the utilization of carbon dioxide and methane by dry reforming. *Appl. Catal. A Gen.* **2009**, *366*, 333–341. [\[CrossRef\]](#)
27. Wang, X.; Chen, Q.; Zhou, Y.; Li, H.; Fu, J.; Liu, M. Cu-based bimetallic catalysts for CO₂ reduction reaction. *Adv. Sens. Energy Mater.* **2022**, *1*, 100023. [\[CrossRef\]](#)

28. Zaza, L.; Rossi, K.; Buonsanti, R. Well-Defined Copper-Based Nanocatalysts for Selective Electrochemical Reduction of CO₂ to C₂Products. *ACS Energy Lett.* **2022**, *7*, 1284–1291. [\[CrossRef\]](#)
29. Chen, C.; Li, Y.; Yu, S.; Louisia, S.; Jin, J.; Li, M.; Ross, M.B.; Yang, P. Cu-Ag Tandem Catalysts for High-Rate CO₂ Electrolysis toward Multicarbon. *Joule* **2020**, *4*, 1688–1699. [\[CrossRef\]](#)
30. Alvarez-Garcia, A.; Flórez, E.; Moreno, A.; Jimenez-Orozco, C. CO₂ activation on small Cu-Ni and Cu-Pd bimetallic clusters. *Mol. Catal.* **2020**, *484*, 110733. [\[CrossRef\]](#)
31. Xing, M.; Guo, L.; Hao, Z. Theoretical insight into the electrocatalytic reduction of CO₂ with different metal ratios and reaction mechanisms on palladium–copper alloys. *Dalt. Trans.* **2019**, *48*, 1504–1515. [\[CrossRef\]](#)
32. Han, L.; Liu, H.; Cui, P.; Peng, Z.; Zhang, S.; Yang, J. Alloy Cu₃Pt nanoframes through the structure evolution in Cu-Pt nanoparticles with a core-shell construction. *Sci. Rep.* **2014**, *4*, 6414. [\[CrossRef\]](#)
33. Jeon, H.S.; Timosnenko, J.; Scholten, F.; Sinev, I.; Herzog, A.; Haase, F.T.; Cuenya, B.R. Operando insight into the correlation between the structure and composition of CuZn nanoparticles and their selectivity for the electrochemical CO₂ reduction. *J. Am. Chem. Soc.* **2019**, *141*, 19879–19887. [\[CrossRef\]](#) [\[PubMed\]](#)
34. Feng, X.; Jiang, K.; Fan, S.; Kanan, M.W. Grain-Boundary-Dependent CO₂ Electroreduction Activity. *J. Am. Chem. Soc.* **2015**, *137*, 4606–4609. [\[CrossRef\]](#) [\[PubMed\]](#)
35. Jiang, X.; Koizumi, N.; Guo, X.; Song, C. Bimetallic Pd-Cu catalysts for selective CO₂ hydrogenation to methanol. *Appl. Catal. B Environ.* **2015**, *170–171*, 173–185. [\[CrossRef\]](#)
36. Megha; Mondal, K.; Ghanty, T.K.; Banerjee, A. Adsorption and Activation of CO₂ on Small-Sized Cu-Zr Bimetallic Clusters. *J. Phys. Chem. A* **2021**, *125*, 2558–2572. [\[CrossRef\]](#)
37. Muthuperianayagam, A.; Azeem, G.N.; -ur-Rehman, A.; Di Tommaso, D. Adsorption, activation, and conversion of carbon dioxide on small copper-tin nanoclusters. *ChemRxiv* **2022**. preprint. [\[CrossRef\]](#)
38. Kabir, M.; Mookerjee, A.; Bhattacharya, A.K. Structure and stability of copper clusters: A tight-binding molecular dynamics study. *Phys. Rev. A-At. Mol. Opt. Phys.* **2004**, *69*, 043203. [\[CrossRef\]](#)
39. Vázquez-Vázquez, C.; Bañobre-López, M.; Mitra, A.; López-Quintela, M.A.; Rivas, J. Synthesis of small atomic copper clusters in microemulsions. *Langmuir* **2009**, *25*, 8208–8216. [\[CrossRef\]](#)
40. Häkkinen, H.; Moseler, M.; Kostko, O.; Morgner, N.; Hoffmann, M.A.; Issendorff, B.V. Symmetry and electronic structure of noble-metal nanoparticles and the role of relativity. *Phys. Rev. Lett.* **2004**, *93*, 093401. [\[CrossRef\]](#)
41. Kleis, J.; Greeley, J.; Romero, N.A.; Morozov, V.A.; Falsig, H.; Larsen, A.H.; Lu, J.; Mortensen, J.J.; Dułak, M.; Thygesen, K.S.; et al. Finite Size Effects in Chemical Bonding: From Small Clusters to Solids. *Catal. Letters* **2011**, *141*, 1067–1071. [\[CrossRef\]](#)
42. Austin, N.; Ye, J.; Mpourmpakis, G. CO₂ activation on Cu-based Zr-decorated nanoparticles. *Catal. Sci. Technol.* **2017**, *7*, 2245–2251. [\[CrossRef\]](#)
43. Austin, N.; Butina, B.; Mpourmpakis, G. CO₂ activation on bimetallic CuNi nanoparticles. *Prog. Nat. Sci. Mater. Int.* **2016**, *26*, 487–492. [\[CrossRef\]](#)
44. Peterson, A.A.; Abild-Pedersen, F.; Studt, F.; Rossmeisl, J.; Nørskov, J.K. How copper catalyzes the electroreduction of carbon dioxide into hydrocarbon fuels. *Energy Environ. Sci.* **2010**, *3*, 1311–1315. [\[CrossRef\]](#)
45. Rossmeisl, J.; Qu, Z.W.; Zhu, H.; Kroes, G.J.; Nørskov, J.K. Electrolysis of water on oxide surfaces. *J. Electroanal. Chem.* **2007**, *607*, 83–89. [\[CrossRef\]](#)
46. Shin, H.; Hansen, K.U.; Jiao, F. Techno-economic assessment of low-temperature carbon dioxide electrolysis. *Nat. Sustain.* **2021**, *4*, 911–919. [\[CrossRef\]](#)
47. Pickard, C.J.; Needs, R.J. Ab initio random structure searching. *J. Phys. Condens. Matter.* **2011**, *23*, 53201. [\[CrossRef\]](#)
48. Xu, Y.; Li, F.; Xu, A.; Edwards, J.P.; Hung, S.F.; Gabardo, C.M.; O'Brien, C.P.; Liu, S.; Wang, X.; Li, Y.; et al. Low coordination number copper catalysts for electrochemical CO₂ methanation in a membrane electrode assembly. *Nat. Commun.* **2021**, *12*, 4–10. [\[CrossRef\]](#)
49. Kresse, G.; Furthmüller, J. Efficient iterative schemes for ab initio total-energy calculations using a plane-wave basis set. *Phys. Rev. B-Condens. Matter Mater. Phys.* **1996**, *54*, 11169–11186. [\[CrossRef\]](#)
50. Mathew, K.; Sundararaman, R.; Letchworth-Weaver, K.; Arias, T.A.; Hennig, R.G. Implicit solvation model for density-functional study of nanocrystal surfaces and reaction pathways. *J. Chem. Phys.* **2014**, *140*, 84106. [\[CrossRef\]](#)
51. Li, H.; Shen, Y.Y.; Du, H.N.; Li, J.; Zhang, H.X.; Xu, C.X. Insight into the mechanisms of CO₂ reduction to CHO over Zr-doped Cu nanoparticle. *Chem. Phys.* **2021**, *540*, 111012. [\[CrossRef\]](#)
52. Chuang, F.C.; Wang, C.Z.; Ho, K.H. Structure of neutral aluminum clusters Al_n (2 ≤ n ≤ 23): Genetic algorithm tight-binding calculations. *Phys. Rev. B-Condens. Matter Mater. Phys.* **2006**, *73*, 125431. [\[CrossRef\]](#)
53. Mao, H.Y.; Li, B.X.; Ding, W.F.; Zhu, Y.H.; Yang, X.X.; Li, C.Y.; Ye, G.X. Theoretical study on the aggregation of copper clusters on a liquid surface. *Materials* **2019**, *12*, 3877. [\[CrossRef\]](#)
54. Holec, D.; Dumitraschkewitz, P.; Fischer, F.D.; Vollath, D. Size-dependent surface energies of Au nanoparticles. *arXiv* **2014**, arXiv:1412.7195.

55. Shin, D.Y.; Won, J.S.; Kwon, J.A.; Kim, M.S.; Lim, D.H. First-principles study of copper nanoclusters for enhanced electrochemical CO₂ reduction to CH₄. *Comput. Theor. Chem.* **2017**, *1120*, 84–90. [[CrossRef](#)]
56. Vogt, C.; Monai, M.; Sterk, E.B.; Palle, J.; Melcherts, A.E.M.; Zijlstra, B.; Groeneveld, E.; Berben, P.H.; Boereboom, J.M.; Hensen, E.J.M.; et al. Understanding carbon dioxide activation and carbon–carbon coupling over nickel. *Nat. Commun.* **2019**, *10*, 5330. [[CrossRef](#)] [[PubMed](#)]
57. Alvarez, S. A cartography of the van der Waals territories. *Dalt. Trans.* **2013**, *42*, 8617–8636. [[CrossRef](#)] [[PubMed](#)]
58. Cordero, B.; Gómez, V.; Platero-Prats, A.E.; Revés, M.; Echeverría, J.; Cremades, E.; Barragán, F.; Alvarez, S. Covalent radii revisited. *J. Chem. Soc. Dalt. Trans.* **2008**, *21*, 2832–2838. [[CrossRef](#)]

Disclaimer/Publisher’s Note: The statements, opinions and data contained in all publications are solely those of the individual author(s) and contributor(s) and not of MDPI and/or the editor(s). MDPI and/or the editor(s) disclaim responsibility for any injury to people or property resulting from any ideas, methods, instructions or products referred to in the content.